Supplementary Information (SI) for Physical Chemistry Chemical Physics.
This journal is © the Owner Societies 2026

Supporting information for

Vibrational memory of anion-modulated water molecules in ultrahigh-concentrated electrolytes

Nicholas Thongbam and Bhabani S. Mallik*

Department of Chemistry, Indian Institute of Technology Hyderabad, Sangareddy-502284, Telangana, India

* bhabani@chy.iith.ac.in

Table S1. The number of species and the obtained densities from the last 10 ns of the NPT simulation for each simulated system.

System	Conc. [m]	HOD	water	Li^+	Cl^-	NO_3^-	*Obtained density [g cm^{-3}]
aq. LiCl	1.0	100	1900	36	36	-	1.026 (0.59)
	5.0	100	1900	181	181	-	1.111 (1.12)
	9.3	100	1900	333	333	-	1.180
	11.1	100	1900	400	400	-	1.191
	13.9	100	1900	500	500	-	1.242
aq. $LiNO_3$	1.0	100	2400	45	-	45	1.041 (0.62)
	5.0	100	2400	226	-	226	1.175 (1.12)
	10.0	100	2400	451	-	451	1.299 (0.62)
	13.0	100	2400	587	-	587	1.358 (0.97)
	15.0	100	2400	677	-	677	1.393 (1.02)

*Density %Error values compared to experimental values[1,2] are provided within brackets

Table S2. Non-bonding parameters used in the simulations

Molecule/ Ion	Atom	σ (Å)	ϵ [kJ mol^{-1}]	Charge [e]
H_2O/ HOD	O_w	3.1644	0.7749	0.0
	H_w	0.0	0.0	0.5564
	D	0.0	0.0	0.5564
	M	0.0	0.0	-1.1128
Li^+	Li	1.8	0.0765	1.0
Cl^-	Cl	4.1	0.4928	-1.0
NO_3^-	N	3.25	0.17	0.905
	O_N	3.00	0.17	-0.635

Table S3. Harmonic bonding parameters used in the simulations

Bonding parameter	Equilibrium value	Force constant
H-O_w-H/D angle	107.4°	367.810 kJ mol^{-1}rad^{-2}
N-O_N bond	0.126 nm	219660 kJ mol^{-1} nm^{-2}
O_N-N-O_N angle	120°	439.320 kJ mol^{-1} rad^{-2}
N-O_N-O_N-O_N improper angle	0°	251.04 kJ mol^{-1} rad^{-2}

Table S4. Morse potential bonding parameters for O_w-H_w/D vibrations

Equilibrium value (r_{eq})	D_r [kJ mol^{-1} nm^{-2}]	β [nm^{-1}]
0.009419 nm	432.58	22.87

Continuous wavelet transform method to calculate instantaneous OD stretching mode frequencies

We encoded the probe HOD molecules' instantaneous OD bond length, $r(t)$ and the instantaneous momentum along the bond, $p(t)$ the real and the imaginary part of a time-series complex function, $f(t)$ for each mode which is given by,

$$f(t) = r(t) + ip(t) \quad (1)$$

We performed continuous wavelet transform on this time-series function, following Arevallo and Wiggins' method of continuous wavelet transform:[3]

$$L_\psi f(a,b) = \frac{1}{\sqrt{a}} \int_{-\infty}^{\infty} f(t)\psi^* \left(\frac{t-b}{a}\right) dt \quad (2)$$

where 'a'and 'b' are the scale and the position parameters of the wavelet. Here, $a > 0, b \in \mathbb{R}$ and the mother wavelet, ψ is a Morlet-Grossman wavelet[4] given by,

$$\psi(t) = \frac{1}{\sigma\sqrt{2\pi}} e^{2\pi i\lambda t} e^{\frac{-t^2}{2\sigma^2}} \quad (3)$$

We assigned λ and σ to be 1 and 2, respectively. The continuous wavelet transform in equation (3) provides the local frequency of $f(t)$ for a small-time window about time, $t = b$, and it can be obtained as:

$$\omega(t=b) = \frac{1}{2a}\left(\lambda + \sqrt{\lambda^2 + \frac{1}{2\pi^2\sigma^2}}\right) \quad (4)$$

The dominant frequency of $f(t)$ at time $t = b$ is given by the maximum modulus of the wavelet transform *i.e.*, $max_a|L_\psi f(a,b)|$. The corresponding frequency was then computed using equation (4). This is the frequency with which the considered OD mode is vibrating at time $t = b$. Thus, the time-dependent bond vibrational frequencies for each OD mode were obtained.

Structural properties

Radial distribution function:

We examined the structural properties of the aq. salt systems. In these systems, the complex and interdependent interactions amongst the species present in the systems define their characteristics. The time-averaged structural arrangements of the ions and water are reflections of these interactions.

Li-Cl radial distribution functions (RDF) were calculated as plotted in Figure S1 along with their corresponding number integral (NI) to study ion interactions in the aq. LiCl systems. In the RDF plots studied, the concentration increase does not change the peak positions, but changes in the peak heights are observed. Prominent first peaks at 0.221 nm are observed, showing strong cation-anion interactions. The second peaks are observed at 0.450 nm with

low peak heights. The peak heights decrease significantly with higher salt concentrations due to an increase in the bulk ion concentration, as inferred from the increased corresponding NI values. The coordination number of the first hydration shell (CN) increases from 0.86 at 1.0 m to 1.94 at 13.9 m. A similar trend in the cation-anion structures is observed in aq. $LiNO_3$. Here, the interaction between Li^+ and O-atoms (O_N) of NO_3^- was examined through the Li-O_N RDF that is presented in Figure S1(b). Overlapping first peaks are located at 0.184 nm with prominent second peaks at 0.389 nm. The first peaks are not as prominent as in the Li-Cl RDFs. A stronger interaction between the ions would manifest as higher peaks in the RDF plot. So, the lower peaks are indications of weaker cation-anion interactions in aq. $LiNO_3$ systems, which is probably due to the more diffuse charge in NO_3^-. The CNs at 1.0 and 15.0 m are 0.64 and 2.45, respectively, which indicates greater ion pairing at higher concentrations, as is seen in aq. LiCl systems.

Apart from the interaction with anions, Li^+ cations get solvated by water. We plot the Li-O_w RDF and NI plots at the various simulated concentrations to study such structures. Again, the peak positions do not change. For aq. LiCl, the plots are shown in Figure S1(c). First peaks occur at 0.198 nm, and second peaks at 0.413 nm. The increase in salt concentration leads to lower NI values and RDF peak heights, where the CN decreases from 3.16 at 1.0 m to 2.06 at 13.9 m. This observation, along with the observed increase in Li^+-anions NI are indication of anions replacing water in the hydration shell of Li^+ at higher concentrations, as reported in previous works.[5] Similar structural trends were observed in the aq. $LiNO_3$ systems. The RDF and NI plots are shown in Figure S1(d). The first peaks are observed at 0.194 nm, and the second peaks at 0.413 nm. The CN is 3.48 at 1.0 m and decreases to 1.78 at 15.0 m, along with slightly lowered peak heights. So, a similar case where ion pairing, which results in less cation-water interaction, is reiterated. Overall, both the aq. systems show very similar Li-O_w RDF profiles and concentration dependence and suggest that the anions show minimal influence on the Li-water interaction.

The anion-water interactions are examined through the Cl-H_w and O_N-H_w RDF and NI plots in S1(e) and (f) for the aq. LiCl and aq. $LiNO_3$ systems, respectively, where no change in peak positions is observed. We observe the first peaks overlapping at 0.215 nm for aq. LiCl systems and at 0.175 nm for aq. $LiNO_3$ systems. The observed doublet second peaks for Cl-H_w RDF occur at 0.348 and 0.422 nm. The first peak of the doublet doesn't change with concentration, whereas the second peak increases with concentration. This suggests an intramolecular origin of the first peak, in particular, the spatial distribution of the other hydrogen, while the second peak might have an intermolecular origin. For O_N-H_w RDFs, the peaks are observed at 0.318 and 0.371 nm. The presence of the doublet in the anion-water RDFs likely arises due to (1) the spatial distribution of other hydrogen, which is not in direct contact with the reference anion, (2) the spatial distribution of the hydrogen bonding hydrogen but with respect to other

reference sites (other O_N), and (3) the approach of anions towards the O-atoms. An angular decomposition of the RDF plots can help further investigate the origin of the observed doublet peaks, as discussed in the analyses below. The NI in both the aq. salt systems were seen to decrease with increased concentrations. The observed higher peaks in Cl-H_w over the peaks in O_N-H_w RDFs and higher NI values indicate stronger anion-water interactions in aq. LiCl systems over the aq. $LiNO_3$ systems. The anion-water structures are further studied through the RDF plots of O_w with reference to the center of mass of anions, as shown in Figure S2(a) for Cl^- and S2(d) for NO_3^-. The Cl-O_w RDF showed a narrower first peak (0.27-39 nm) than N-O_w RDFs (0.28-0.49 nm), suggesting stronger ionic interactions in the former. Cl-O_w RDF also exhibited a doublet (0.31 and 0.34 nm) in the first solvation shell at higher concentrations. The closer peak is attributed to the distance between the hydrogen bond donor, O_w, and acceptor Cl^-. The second doublet peak has been attributed to a Cl-Li-O linkage. Here, the Cl and O atoms are part of coordination tetrahedra of Li, which becomes more significant at higher concentrations.[5] The N-O_w RDFs showed the first peak at ~0.35 nm. The RDF suggests that the hydration shells become more structured with an increase in concentration. This is distinctly evident at 1.0 m, where the second peak and beyond are not prominent. The lower number of NO_3^- and their weak interaction with water may be responsible for the observed profile. Besides this, the peaks do not show any concentration-dependent trend, which suggests weak water structure modulation by NO_3^-. For both anions, the corresponding NI values decrease with concentration, which likely stems from increased Li-anion ion pairing.

The O_w-O_w and O_w-H_w RDFs are also plotted to study the water-water interaction in the aq. salt solutions. The first peaks of both the RDFs showed concentration-dependent decrease in height in aq. LiCl solutions (Figure S2(b,c)). This suggests inter-water solvation shell disruption due to the ions. Such a decrease is very low in aq. $LiNO_3$ solutions (Figure S2 (e,f)), which shows a lower disruptive strength of NO_3^-. The O_w-O_w RDF profile becomes less prominent beyond the first solvation shell, especially at higher concentrations, which is most likely due to the interruption of inter-water interaction by ions. In the case of the O_w-H_w RDFs, the higher ion concentration appears to help align the other hydrogen from the observed increase in definition of the humps and valleys from the second solvation shell for both salt solutions. A small shoulder definition also forms at ~0.38 nm at concentrations above 1.0 m, which likely arises from ion interruptions to inter-water interactions.

Spatial distribution function:

We further examined the distribution of the cations and anions around water molecules through the spatial distribution function (SDF) plots for the aq. LiCl and aq. $LiNO_3$ systems as presented in Figure S1(g) and (h), respectively. All the SDF plots were plotted with an isosurface value of 20 species/nm^{-3}. For NO_3^-, the SDF was plotted based on the distribution

of its center of mass. It was seen that Li^+ cations were localized near the O-atom of water and were spread along the bisector of water. This is due to the greater negative charge on the O-atom. The anions, meanwhile, were distributed near the more positive H-atoms. The NO_3^- distributions were spread over a larger space in comparison to Cl^-. Such ion distributions about water are mainly caused by the water-ion H-bond interactions. The wider spatial spread observed for NO_3^- might be due to the bulkier nature of the anion with its multiple interacting sites (three O-atoms) that enables a greater range of orientational configuration around the water molecules. At higher ion concentrations, an increased distribution of counter-ions of the first shell cations and anions is expected. For the aq. LiCl systems, this distribution manifested in the SDF plots as a second layer, which becomes more prominent with an increase in concentration, but for aq. $LiNO_3$ systems, the SDF plots with the same isovalue did not show the second layer distributions. This is a further indication of weaker cation-anion interactions in aq. $LiNO_3$ systems. A stronger cation-anion interaction would allow the first shell ions around water to pull in their counter-ions closer. This increases the SDF density of the second shell.

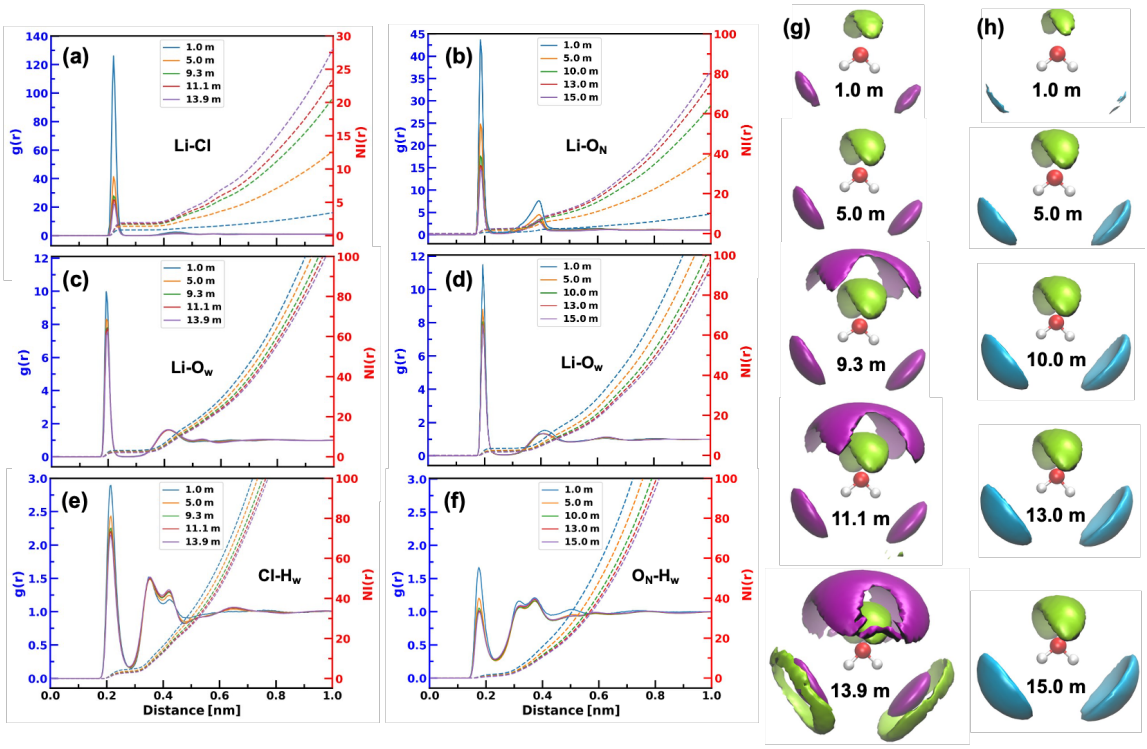

Figure S1. Radial distribution function (RDF) and number integral (NI) plots of (a) Li-Cl, (b) Li-O_N, (c) Li-O_w (aq. LiCl), (d) Li-O_w (aq. $LiNO_3$), (e) Cl-O_w and (f) O_N-H_w pairs of aq. LiCl and $LiNO_3$ systems at different concentrations. The RDFs and NIs are plotted with solid and dashed lines, respectively. Spatial distribution function (SDF) plots of (g) Li^+ (green) and Cl^- (purple) around water for aq. LiCl systems and (h) Li^+ and NO_3^- (cyan) around water for aq. $LiNO_3$ systems at the labelled concentrations. The isosurface value for all the SDF plots is 20 species/nm^{-3}.

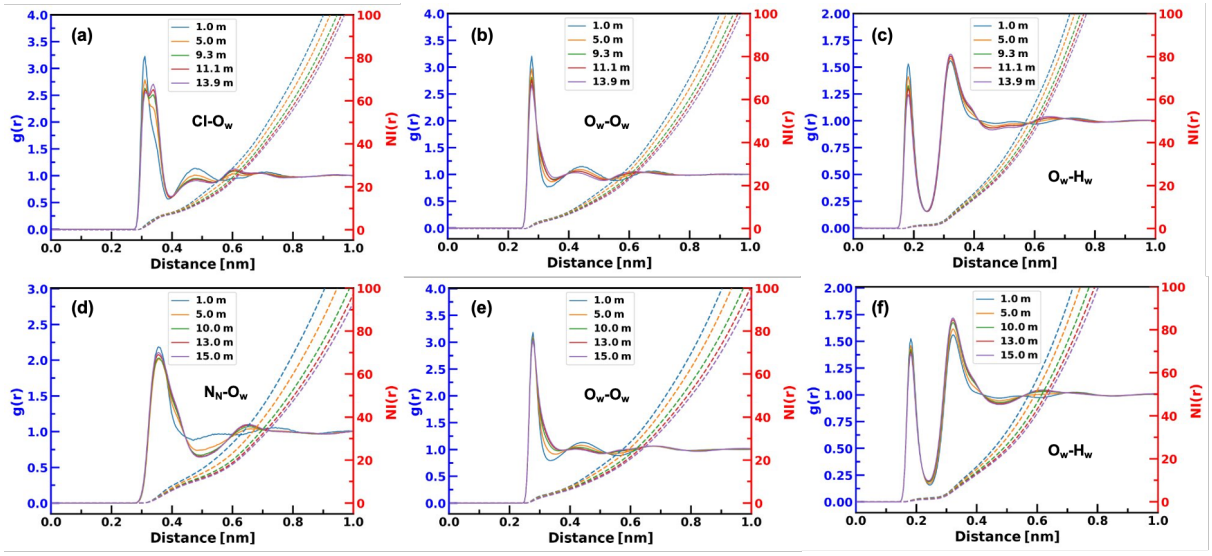

Figure S2. RDF and NI plots for (a-c) aq. LiCl and (d-f) aq. $LiNO_3$ systems. The Cl-O_w and N-O_w RDF and NI plots are shown in (a) and (b), respectively. (b) and (e) shows the O_w-O_w RDF and NI plots for aq. LiCl and aq. $LiNO_3$ systems, respectively. (c) and (f) shows the O_w-H_w RDF and NI plots for aq. LiCl and aq. $LiNO_3$ systems, respectively.

Combined distribution function:

We further delve into the structural features of the H-bonding structures. These are constituted by the anion-water and inter-water pairs found in the aq. salt systems. For that purpose, we calculated the combined distribution functions (CDF) for H-bonding pairs: 1) Cl^--water, 2) inter-water, and 3) NO_3^--water, as shown in Figure S3. The CDFs are calculated for the distance, R, and the H-bond angle, θ. Here, 'R' is the distance from the H-bond acceptor to the corresponding H-atom, while 'θ' is the angle made between the two vectors having a common base at the H-bonded H-atom with their tips at the H-bond donor and acceptor atoms, respectively.

Figure S3(a) and (b) show the CDF plots for the Cl^--water pairs at 1.0 and 13.9 m, respectively, representing the lowest and the highest concentrations studied here. The CDF plots for the remaining concentrations are shown in Figures S4-5. The observed prominent contours near 0.2 nm and the angular region of 135-180° correspond to the first hydration shell of Cl^- anions. They describe the geometrical properties of Cl^--water H-bond. The spatial distribution of the other H-atom of water results in the contours around the 0.3 nm region and the angular region 45-90°. This corresponds to the first peak of the doublet's second peak in the Cl-H_w RDF. In the case of the anion-water CDF, corresponding to the second peak of the Cl-H_w RDF's doublet, there are contours around 0.4 nm in the angular region 0-30° at higher concentrations. This might indicate the presence of Cl^- anions approaching the water molecules towards the O-atom due to molecular crowding at high concentrations. Furthermore, the Li situated near the O-atoms will help with this Cl^- approach. Such assistance is evident from the increasing RDF peak height at 0.4 nm with concentration and the increased Cl density observed in the SDF

plots, as higher concentrations increase the propensity to form contact ion pairs. Inter-water CDF plots for aq. LiCl systems are presented in Figures S3(c) and (d) for the above salt concentrations. The distributions of the prominent contours were similar to the Cl^--water CDF plots. The prominent contours in the 135-180° angular region near 0.2 nm correspond to the inter-water H-bond configurations. The distributions of the other H-atom contribute to the contours near 0.3 nm. These contours correspond to the second peaks observed in the inter-water RDF shown in Figure S2(c). The observed features for the inter-water CDF plots can also be seen in aq. $LiNO_3$ systems (Figures S2 (e) and (f)). For the NO_3^--water CDF plots as shown in Figures S3(g,h) for 1.0 and 15.0 m, respectively, the H-bonded configuration of H-atoms and O-atom of NO_3^- occurred with a radial distance around 0.2 nm with a slightly larger angular distribution in the region ~140-180°, indicating less rigidity in their structural configurations. Contours were also observed around 0.4 nm over a larger angular region, but with higher prominence around 150-180°. These describe the distribution of the H-atoms with respect to the other two O-atoms of the NO_3^- anion. They also correspond to the second peaks observed in the anion-water and inter-water RDFs. The second hydration shell distribution of anions discussed for Cl^- will be less prominent for the more diffuse NO_3^- anion, and it is also not evident from the same O_N-H_w RDF peak height at 0.4 nm over all concentrations, and the less prominent contour at the same distance with angle distribution near 0°. Overall, from the CDF plots of aq. $LiNO_3$ and aq. LiCl systems, we can infer a more dispersed distribution of water around NO_3^- anions versus a more rigid Cl^--water structure, while the inter-water structures are quite similar.

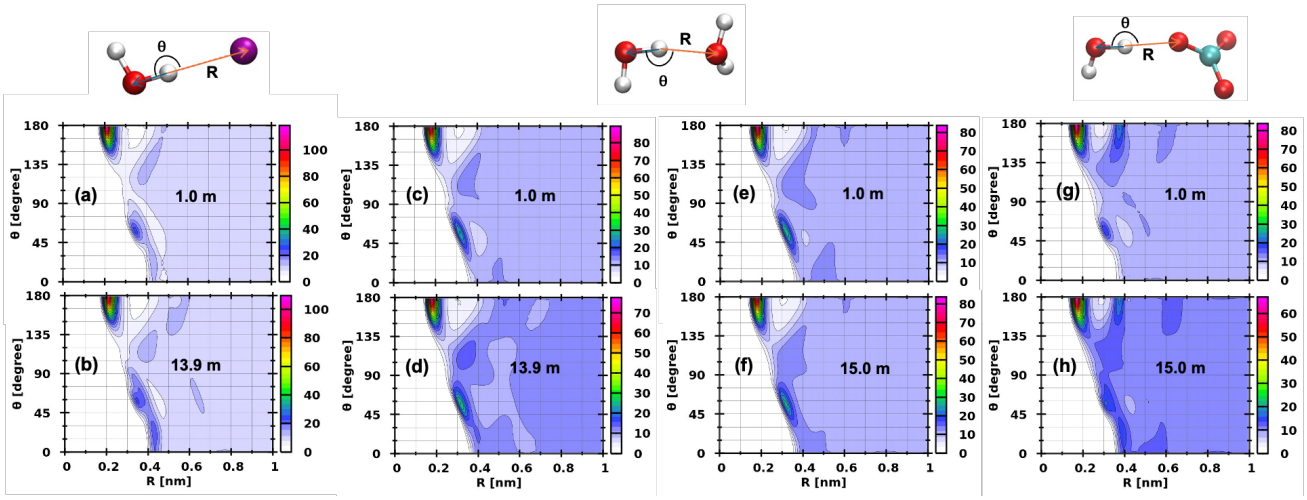

Figure S3. Combined distribution function (CDF) plots of H-bonding pairs: (a,b) Cl^--water, (c,d) inter-water for 1.0 and 13.9 m aq. LiCl systems, respectively, (e,f) inter-water and (g,h) NO_3^--water for 1.0 and 15.0 m aq. $LiNO_3$ systems, respectively. The schematic representations above the plots illustrate the geometrical parameters used for the respective CDF plots.

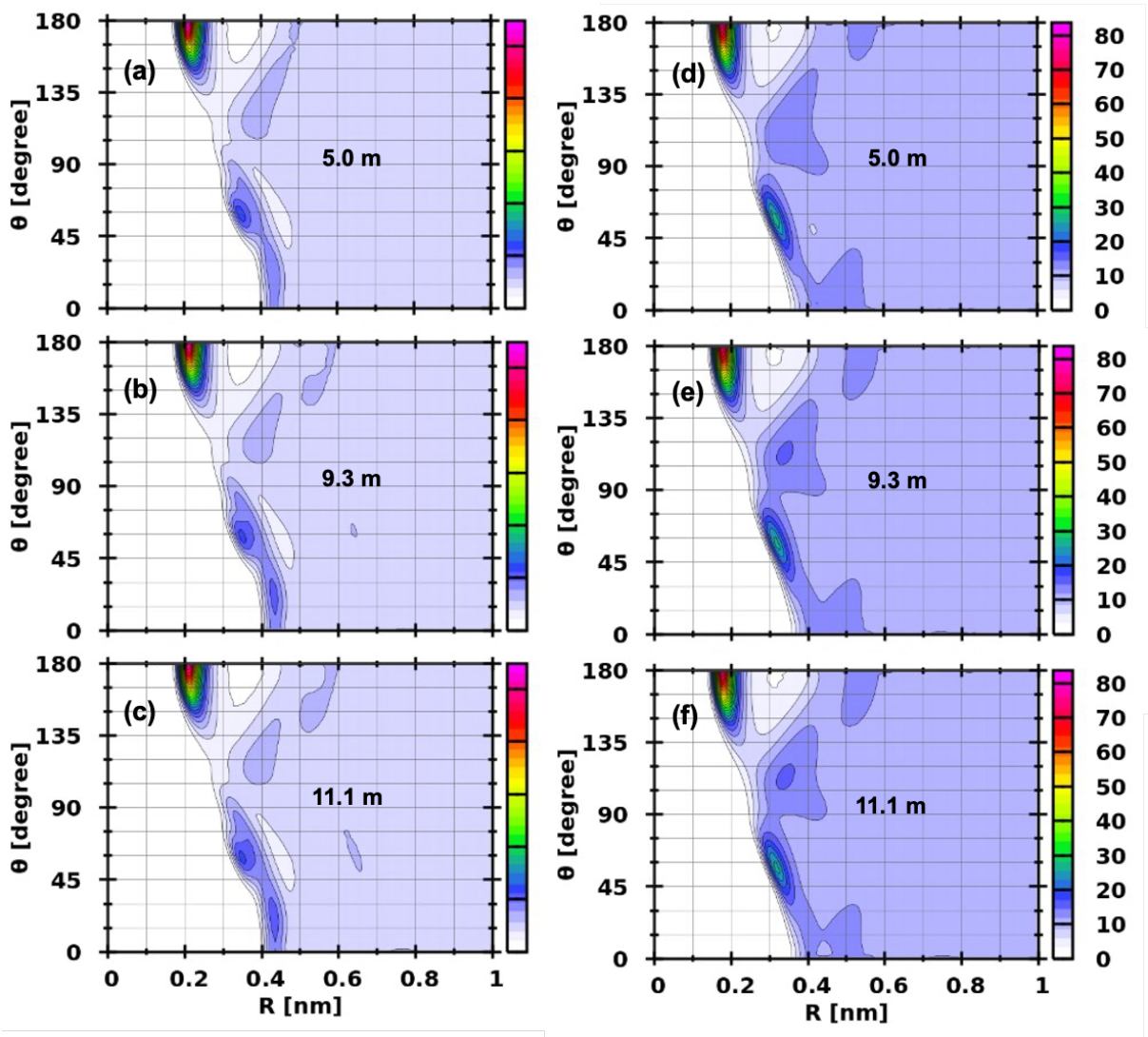

Figure S4. Combined distribution function (CDF) plots of H-bonding pairs: (a-c) Cl^--water, (d-f) water-water for 5.0, 9.3, and 11.1 m aq. LiCl systems, respectively.

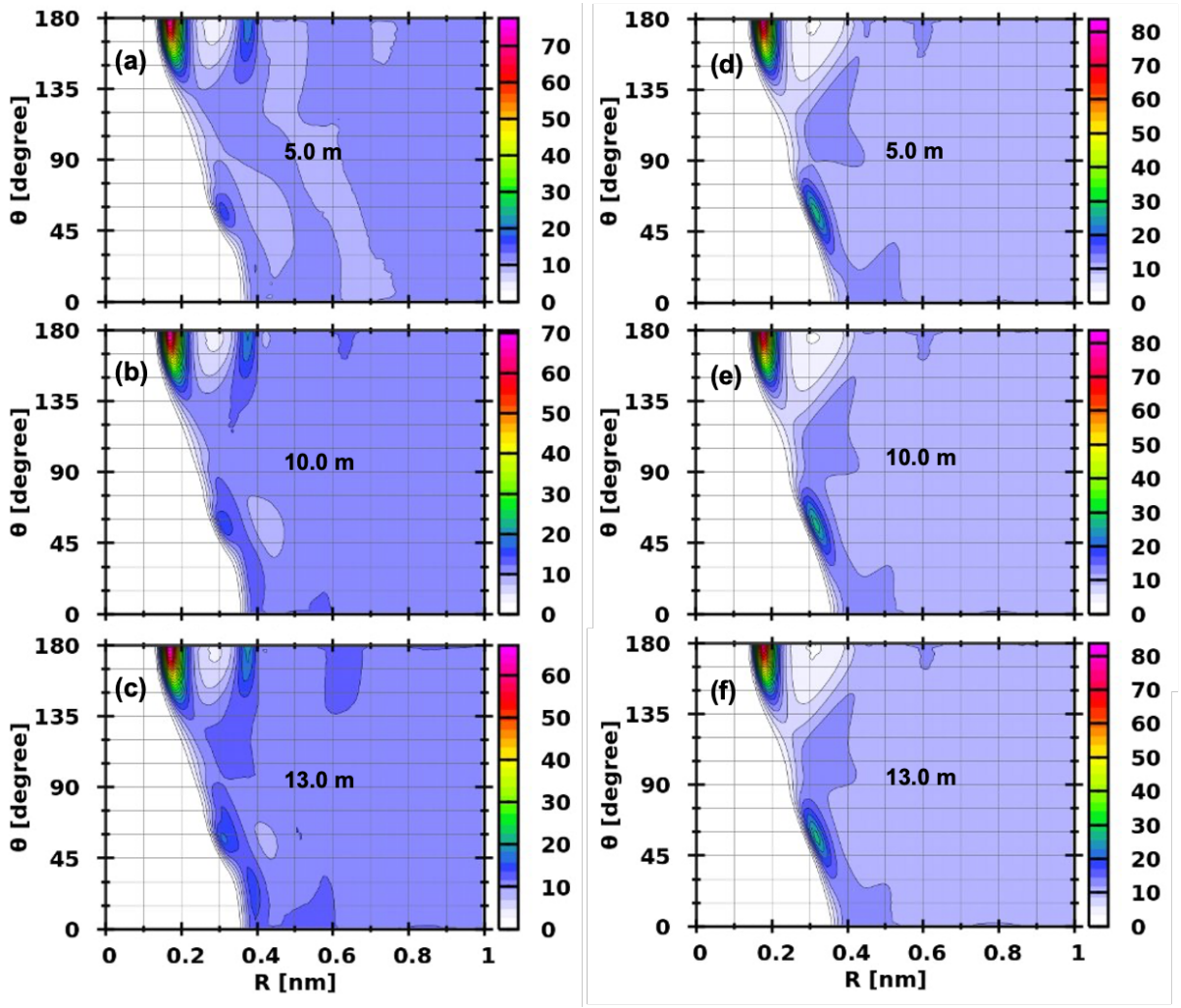

Figure S5. Combined distribution function (CDF) plots of H-bonding pairs: (a-c) NO_3^--water, (d-f) water-water for 5.0, 10.0, and 13.0 m aq. $LiNO_3$ systems, respectively

Mean-squared displacement (MSD)

The mean-squared displacements (MSDs) of the various species (Li^+, Cl^-, NO_3^-, H_2O) present in the aqueous systems are presented in Figure S6. The MSD is given by:

$$\mathbf{MSD} = \frac{\mathbf{1}}{\boldsymbol{N}}\sum_{\boldsymbol{i=1}}^{\boldsymbol{N}}[\boldsymbol{r_i(t)} - \boldsymbol{r_i(0)}]^2 \qquad (5)$$

here, for a species, the position of the i^{th} particle at time '$\boldsymbol{t}$' is given by $\boldsymbol{r_i(t)}$ and '$\boldsymbol{N}$ is the total number of particles. The MSD plots report on the translational diffusivity of the particles. In the diffusive regime the ln(MSD) vs. ln ($\boldsymbol{t}$) plot is linear with a slope of '1'. This slope is called the $\boldsymbol{\beta}$ value and it is evaluated as:[6]

$$\boldsymbol{\beta(t)} = \frac{\boldsymbol{d}\,\mathbf{ln}(\boldsymbol{MSD})}{\boldsymbol{d}\,\mathbf{ln}(\boldsymbol{t})} \qquad (6)$$

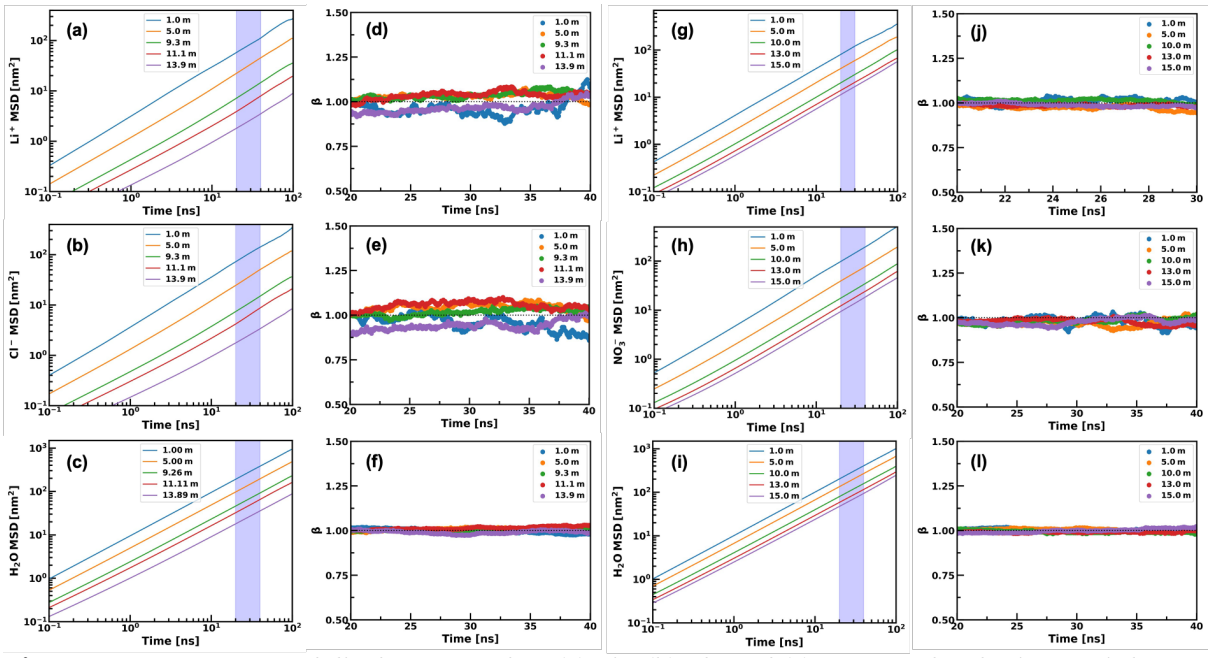

Figure S6. Mean-squared displacement plots (a) Li^+, (b) Cl^-, and (c) water molecules in aq. LiCl systems and their corresponding β plots over their diffusive regions are shown in (d-f), respectively. Similarly, for aq. $LiNO_3$ systems, MSD plots (g) Li^+, (h) NO_3^-, and (i) water molecules, and their corresponding β plots over their diffusive regions are shown in (j-l), respectively.

Table S5. The fitting parameters for the tri-exponential fits to the ($C_\omega(t)$ decay curve of the aq. salt systems.

System	Conc. [m]	a_1	a_2	τ_1 [ps]	τ_2 [ps]	τ_3 [ps]	R^2
aq. LiCl	1.0	0.716	0.211	0.047	0.662	2.505	0.990
	5.0	0.668	0.182	0.050	0.590	3.179	0.992
	9.3	0.697	0.176	0.052	0.965	5.122	0.989
	11.1	0.683	0.157	0.053	1.227	8.383	0.983
	13.9	0.683	0.153	0.056	1.361	8.819	0.989
aq. $LiNO_3$	1.0	0.688	0.204	0.045	0.446	1.884	0.990
	5.0	0.654	0.225	0.050	0.567	3.221	0.975
	10.0	0.650	0.202	0.050	0.564	3.583	0.983
	13.0	0.650	0.185	0.054	0.670	3.996	0.978
	15.0	0.621	0.155	0.050	0.476	4.055	0.944

Table S6. Fitting parameters of the stretched mono-exponential fit to the $C_2(t)$ decay in the aq. salt systems

System	Conc. [m]	a_0	τ [ps]	β	R^2
aq. LiCl	1.0	0.844	2.956	0.782	0.999
	5.0	0.880	4.181	0.658	0.999
	9.3	0.888	6.331	0.595	0.999
	11.1	0.895	8.290	0.559	0.999
	13.9	0.927	10.499	0.483	0.999
aq. $LiNO_3$	1.0	0.842	2.728	0.792	0.999
	5.0	0.852	2.950	0.734	0.999
	10.0	0.869	3.324	0.660	0.999
	13.0	0.878	3.624	0.622	0.999
	15.0	0.882	3.840	0.603	0.999

Hydrogen bond (H-bond) dynamics

We followed Luzar and Chandler's method to calculate the H-bond correlation functions.[7,8] The calculated decay plots of the H-bond correlation functions for the different aq. systems and their corresponding stretched mono-exponential fits are shown in Figure 5. The fitting

parameters for the aq. LiCl systems are given in Table S7, while those for aq. $LiNO_3$ systems are provided in Table S8.

The population correlation function uses the hydrogen bond population variables $\boldsymbol{h}(\boldsymbol{t})$ and $\boldsymbol{H}(\boldsymbol{t})$. For a given pair H-bonded at the time $\boldsymbol{t} = \boldsymbol{0}$, $\boldsymbol{h}(\boldsymbol{t})$ takes the value '1' if they are also H-bonded at a time '$\boldsymbol{t}$' and '0' otherwise. $\boldsymbol{H}(\boldsymbol{t})$ takes the value '0' if the H-bonding remains continuously intact till a time '$\boldsymbol{t}$' and '0' otherwise. We used only the distance criteria to determine whether the pairs are H-bonded or not. In the above inter-water and anion-water CDF plots, we have observed that the angular distributions of the first hydration shells were localized in the region ~135-180°, although with some outliers. This shows that the inter-molecular configurations mostly stay within the angular range of 135-180° in the first hydration shells. We take note of these observations to use a less strict geometry metric for our H-bond definition. This may also help account for fast libration motions that produce intermittent strained angular configurations without rupturing the H-bond.[9] The distance cutoffs (r_{cut}) were determined from the first minima of the H-bond acceptor atom and H/D-atom RDF plots presented in Figure S1(c, f) and S2(c, f), respectively for the Cl^--water, NO_3^--water, inter-water (aq. LiCl), and inter-water (aq. $LiNO_3$) pairs. Their corresponding values of r_{cut} were 0.282, 0.236, 0.245, and 0.245 nm. We calculated the continuous ($\boldsymbol{S_{HB}}(\boldsymbol{t})$) and the intermittent H-bond correlation functions ($\boldsymbol{C_{HB}}(\boldsymbol{t})$) which are given by:

$$\boldsymbol{S_{HB}}(\boldsymbol{t}) = \frac{\langle \boldsymbol{H}(\boldsymbol{t})\boldsymbol{h}(\boldsymbol{0})\rangle}{\langle \boldsymbol{h}(\boldsymbol{0})^2\rangle} \tag{7}$$

$$\boldsymbol{C_{HB}}(\boldsymbol{t}) = \frac{\langle \boldsymbol{h}(\boldsymbol{t})\boldsymbol{h}(\boldsymbol{0})\rangle}{\langle \boldsymbol{h}(\boldsymbol{0})^2\rangle} \tag{8}$$

$\boldsymbol{S_{HB}}(\boldsymbol{t})$ measures how long the H-bonds are continuously maintained after their formation. However, after the H-bond ruptures, the involved species may stay close by and reform the H-bond. $\boldsymbol{C_{HB}}(\boldsymbol{t})$ account for the durations of such sustained H-bonds with intermittent disruptions. So, the obtained decay timescales for the $\boldsymbol{S_{HB}}(\boldsymbol{t})$ and the $\boldsymbol{C_{HB}}(\boldsymbol{t})$ give the H-bond lifetime and relaxation time, respectively.

Table S7. Fitting parameters of the stretched mono-exponential fit to the $S_{HB}(t)$ and $C_{HB}(t)$ decay for Cl^--water and water-water interactions in the aq. LiCl systems

Corr. type	Conc. [m]	Cl^--water				Water-water			
		a_0	τ [ps]	β	R^2	a_0	τ [ps]	β	R^2
Cont.	1.0	0.979	3.196	0.916	0.999	0.974	1.532	0.871	0.999
	5.0	0.987	3.317	0.817	0.999	0.981	1.586	0.810	0.999
	9.3	0.997	3.480	0.752	0.999	0.991	1.614	0.752	0.999
	11.1	1.010	3.761	0.712	0.999	1.002	1.651	0.722	0.999
	13.9	1.017	3.751	0.663	0.999	1.012	1.611	0.679	0.999
Int.	1.0	1.010	18.490	0.709	0.999	1.013	5.624	0.682	0.999
	5.0	0.989	29.478	0.668	0.999	1.009	7.359	0.624	0.999
	9.3	0.962	49.943	0.650	0.999	0.982	10.692	0.596	0.999
	11.1	0.966	76.327	0.605	0.999	0.967	14.337	0.584	0.999
	13.9	0.956	148.059	0.533	0.999	0.967	19.050	0.522	0.999

Table S8. Fitting parameters of the stretched mono-exponential fit to the $S_{HB}(t)$ and $C_{HB}(t)$ decay for NO_3^--water and water-water interactions in the aq. $LiNO_3$ systems

Corr. type	Conc. [m]	NO_3^--water				water-water			
		a_0	τ [ps]	β	R^2	a_0	τ [ps]	β	R^2
Cont.	1.0	0.984	1.269	0.874	0.999	0.974	1.502	0.869	0.999
	5.0	0.990	1.139	0.794	0.999	0.973	1.455	0.837	0.999
	10.0	1.006	0.997	0.723	0.999	0.977	1.429	0.795	0.999
	13.0	1.012	0.974	0.698	0.999	0.982	1.409	0.765	0.999
	15.0	1.020	0.953	0.681	0.999	0.983	1.397	0.749	0.999
Int.	1.0	1.043	10.204	0.564	0.999	0.985	5.604	0.724	0.999
	5.0	1.034	11.550	0.508	0.999	0.985	5.937	0.675	0.999
	10.0	0.992	16.296	0.476	0.999	0.983	6.958	0.622	0.999
	13.0	0.978	21.268	0.454	0.999	0.986	7.705	0.584	0.999
	15.0	0.978	23.751	0.438	0.999	0.974	8.712	0.574	0.999

Hydration shell dynamics

The continuous ($\mathbf{S_{IC}(t)}$) and intermittent ($\mathbf{C_{IC}(t)}$) hydration shell correlation functions are given by:

$$\boldsymbol{S_{IC}(t) = \frac{\langle H(t)h(0)\rangle}{\langle h(0)^2\rangle}} \quad (9)$$

$$\boldsymbol{C_{IC}(t) = \frac{\langle h(t)h(0)\rangle}{\langle h(0)^2\rangle}} \quad (10)$$

where, the population variable $\boldsymbol{H(t)}$ is valued '1' if the constitution of the first hydration shell of the solute is preserved throughout the time '$\boldsymbol{t}$', and '0' otherwise. For $\boldsymbol{h(t)}$, its value is '1' if the constitution of the first hydration shell of the solute is preserved at time 't', with intermittent changes allowed, and '0' otherwise. The boundaries of the first hydration shells were determined from the positions of the first minima of the center-of-mass-based RDFs of Cl^--water, NO_3^--water, inter-water (in aq. LiCl and $LiNO_3$ systems), as shown in Figure S2(a, b, d, and e), respectively. The $\mathbf{S_{IC}(t)}$ and $\mathbf{C_{IC}(t)}$ decay plots for the anion-water and inter-water interactions for the various salt systems have been presented in Figure 6, and their corresponding stretched mono-exponential fits are given in Table S9-10.

Table S9. Fitting parameters of the stretched mono-exponential fit to the $S_{IC}(t)$ and $C_{IC}(t)$ decay for Cl^--water and water-water interactions in the aq. LiCl systems

Corr. type	Conc. [m]	Cl^--water				water-water			
		a_0	τ [ps]	β	R^2	a_0	τ [ps]	β	R^2
Cont.	1.0	0.916	7.144	0.941	0.999	0.873	2.925	0.810	0.999
	5.0	0.921	8.077	0.852	0.999	0.879	3.021	0.747	0.999
	9.3	0.924	9.215	0.798	0.999	0.887	3.158	0.693	0.999
	11.1	0.936	10.091	0.760	0.999	0.897	3.344	0.667	0.999
	13.9	0.944	10.986	0.708	0.999	0.912	3.290	0.613	0.999
Int.	1.0	0.998	41.326	0.559	0.999	1.001	8.198	0.532	0.999
	5.0	0.961	129.525	0.553	0.999	1.018	13.908	0.452	0.999
	9.3	0.946	242.163	0.570	0.999	0.960	30.325	0.454	0.999
	11.1	0.943	385.743	0.581	0.999	0.947	46.403	0.444	0.999
	13.9	0.945	945.470	0.508	0.999	0.904	85.916	0.455	0.999

Table S10. Fitting parameters of the stretched mono-exponential fit to the $S_{IC}(t)$ and $C_{IC}(t)$ decay for NO_3^--water and water-water interactions in the aq. $LiNO_3$ systems

Corr. type	Conc. [m]	NO_3^--water				water-water			
		a_0	τ [ps]	β	R^2	a_0	τ [ps]	β	R^2
Cont.	1.0	0.911	5.868	0.654	0.999	0.855	3.113	0.729	0.999
	5.0	0.920	8.692	0.645	0.999	0.874	3.169	0.687	0.999
	10.0	0.917	12.159	0.648	0.999	0.887	3.399	0.652	0.999
	13.0	0.915	14.448	0.646	0.999	0.894	3.536	0.635	0.999
	15.0	0.915	15.252	0.644	0.999	0.894	3.779	0.628	0.999
Int.	1.0	0.925	27.692	0.619	0.999	0.902	10.054	0.598	0.999
	5.0	0.928	54.582	0.630	0.999	0.902	14.474	0.574	0.999
	10.0	0.928	97.454	0.648	0.999	0.893	22.766	0.566	0.999
	13.0	0.934	137.602	0.630	0.999	0.890	30.675	0.556	0.999
	15.0	0.933	162.804	0.631	0.999	0.888	39.007	0.554	0.999

Pearson correlation coefficient

The Pearson correlation coefficient (r) between two variables, X and Y is given by:

$$r = \frac{\sum_{i=1}^{n}(X_i - \bar{X})(Y_i - \bar{Y})}{\sqrt{\sum_{i=1}^{n}(X_i - \bar{X})^2}\sqrt{\sum_{i=1}^{n}(Y_i - \bar{Y})^2}} \quad (11)$$

$\boldsymbol{r}$ ranges from -1 to 1, corresponding to the highest negative and positive linear correlations. An $\boldsymbol{r}$ value of '0' indicates no linear correlation between the variables taken.

Non-charge scaling

The use of charge scaling through the electronic continuum correction for Li and Cl forcefields reportedly improves the aqueous solution structure with reference to NDIS (neutron diffraction with isotopic substitution) results.[10,11] Pluhařová *et al.* scaled the charge on these ions to 0.75 and -0.75, respectively. In our simulations, it is observed that the $C_\omega(t)$ plot showed faster decay due to charge-scaling (Figure S7). The long timescale of spectral diffusion (τ_3) at 11.1 m aq. LiCl solution is significantly faster (3.15 ps) than the experimental values of ~11 ps reported by Roget *et al.*[12] The fitting parameters are presented in Table S11. This might be due to the slightly higher self-diffusion coefficient of ions and water as evaluated by Pethes[13] and weaker inter-species interactions, which originate from the charge scaling. Faster translational motions will lead to lower τ_3 values, as it reports on the timescale of complete hydrogen bond reorientation. When taking the full ionic charges (Table S1), the MSD of the ions was ~10 times lower, and for water, it was less by ~2 times (Figure S8). Also, the τ_3 values showed better agreement with experimental values, although it is still lower for higher salt concentrations, as discussed in the main text.

We compared the LiCl, Li-O_w, and the Cl-H_w RDF and NI plots (Figure S9) to analyze the structural difference of the LiCl salt solutions between the charge-scaled and full ionic charge simulations. The less prominent Li-Cl RDF peaks and lower NI plots (Figure S9(a)) indicate lower contact ion pair formation in the charge-scaled simulation. The first peak was shifted by +0.014 nm and occurred at 0.235 nm. There were no prominent peaks after the second peak, which was observed as a bump at ~0.58 nm in the full charge simulation Li-Cl RDF plot. Overall, the ion-ion interaction showed greater structuring when ions' full charges were taken. This structuring was less prominent in ion-water structures (Figure 9(b,c)). The charge-scaled and full charge simulations showed the Li-O_w first peak at 0.198 nm, with similar NI plots. The charge-scaled Cl-H_w RDF's first peak occurred at 0.221 nm, which is a shift of 0.006 nm. The peaks were slightly broader when charge-scaled, with some difference in the second peak, but the NI plots again showed minor differences.

Hence, we can affirm that some notable cation-anion and ion-water structural changes occur when using full ionic charges, but they are less prominent for the ion-water structures. Since

the scope of our work is to correlate the vibrational dynamics of the salt systems with their underlying molecular dynamics, we undertook the compromise in modelling to retain the full ionic charges in our simulations, which gave spectral diffusion timescales closer to spectroscopy experiments, with some tradeoff for structure and diffusion.

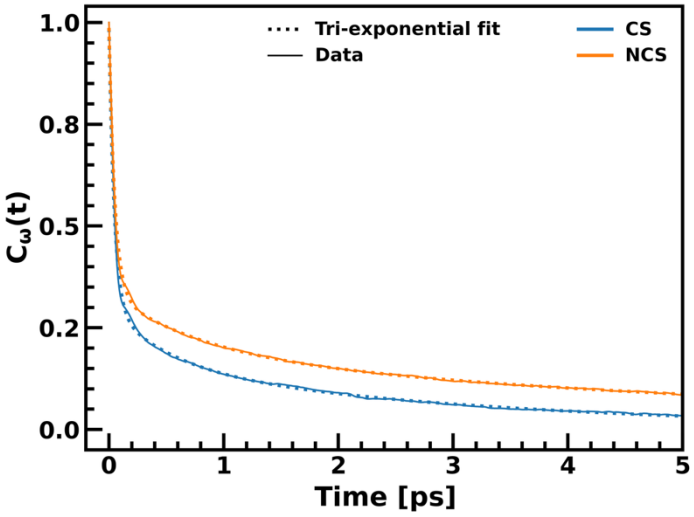

Figure S7. Comparative OD stretching mode's $C_\omega(t)$ plots of charge-scaled (CS) and non-charge-scaled (NCS) simulations of 11.1 m aq. LiCl solution.

Table S11. The fitting parameters for the tri-exponential fits to the ($C_\omega(t)$ decay curve of the 11.1 m aq. LiCl solution for charge-scaled (CS) and non-charge scaled (NCS) simulations.

Simulation	a_1	a_2	τ_1 [ps]	τ_2 [ps]	τ_3 [ps]	R^2
NCS	0.683	0.157	0.053	1.227	8.383	0.983
CS	0.663	0.149	0.050	0.780	3.150	0.998

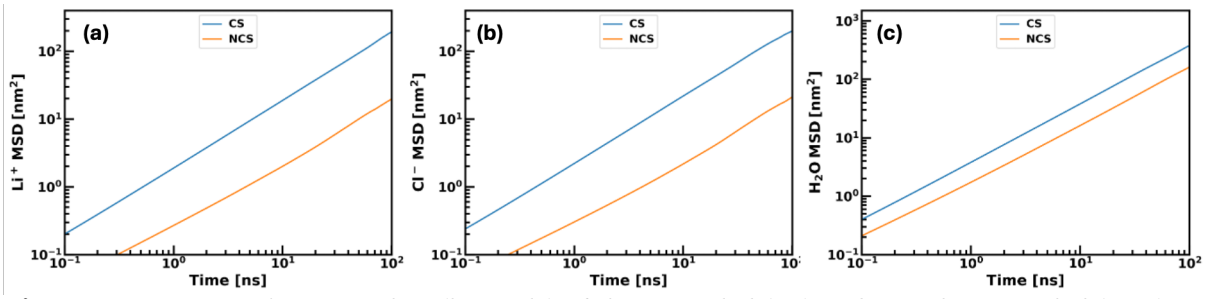

Figure S8. Comparative MSD plots (log scale) of charge-scaled (CS) and non-charge-scaled (NCS) simulations of 11.1 m aq. LiCl solution. (a) Li, (b) Cl, and (c) H_2O

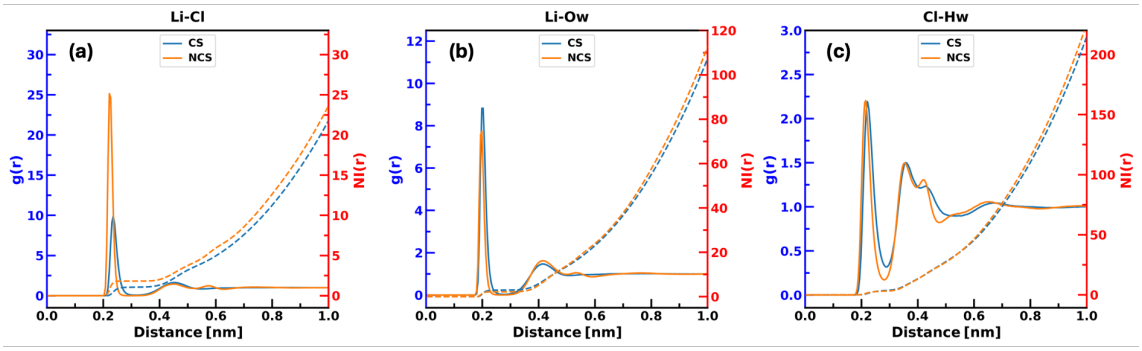

Figure S9. Comparative RDF plots of charge-scaled (CS) and non-charge-scaled (NCS) simulations of 11.1 m aq. LiCl solution. (a) Li-Cl, (b) Li-O_w, and (c) Cl-H_w, where Ow and Hw are atoms of water.

REFERENCES

(1) Zhang, M.; Gao, Y.; Fu, L.; Bai, Y.; Mukherjee, S.; Chen, C.-L.; Liu, J.; Bian, H.; Fang, Y. Chain-like Structures Facilitate Li^+ Transport in Concentrated Aqueous Electrolytes: Insights from Ultrafast Infrared Spectroscopy and Molecular Dynamics Simulations. *J. Phys. Chem. Lett.* **2023**, *14* (31), 6968–6976. https://doi.org/10.1021/acs.jpclett.3c01494.

(2) Zhang, M.; Peng, J.; Gao, Y.; Wang, B.; He, J.; Bai, Y.; Liu, J.; Chen, C.-L.; Fang, Y.; Bian, H. Unveiling the Structural and Dynamic Characteristics of Concentrated $LiNO_3$ Aqueous Solutions through Ultrafast Infrared Spectroscopy and Molecular Dynamics Simulations. *J. Phys. Chem. Lett.* **2024**, *15* (30), 7610–7619. https://doi.org/10.1021/acs.jpclett.4c01449.

(3) Vela-Arevalo, L. V.; Wiggins, S. Time-Frequency Analysis of Classical Trajectories of Polyatomic Molecules. *Int. J. Bifurcation Chaos* **2001**, *11* (05), 1359–1380. https://doi.org/10.1142/S0218127401002766.

(4) Grossmann, A.; Morlet, J. Decomposition of Hardy Functions into Square Integrable Wavelets of Constant Shape. *SIAM Journal on Mathematical Analysis* **1984**, *15* (4), 723–736. https://doi.org/10.1137/0515056.

(5) Pethes, I. The Structure of Aqueous Lithium Chloride Solutions at High Concentrations as Revealed by a Comparison of Classical Interatomic Potential Models. *Journal of Molecular Liquids* **2018**, *264*, 179–197. https://doi.org/10.1016/j.molliq.2018.05.044.

(6) Del Pópolo, M. G.; Voth, G. A. On the Structure and Dynamics of Ionic Liquids. *J. Phys. Chem. B* **2004**, *108* (5), 1744–1752. https://doi.org/10.1021/jp0364699.

(7) Luzar, A.; Chandler, D. Hydrogen-Bond Kinetics in Liquid Water. *Nature* **1996**, *379* (6560), 55–57. https://doi.org/10.1038/379055a0.

(8) Luzar, A.; Chandler, D. Effect of Environment on Hydrogen Bond Dynamics in Liquid Water. *Phys. Rev. Lett.* **1996**, *76* (6), 928–931. https://doi.org/10.1103/PhysRevLett.76.928.

(9) Zeng, Y.; Jia, Y.; Yan, T.; Zhuang, W. Binary Structure and Dynamics of the Hydrogen Bonds in the Hydration Shells of Ions. *Phys. Chem. Chem. Phys.* **2021**, *23* (19), 11400–11410. https://doi.org/10.1039/D0CP06397E.

(10) Pluhařová, E.; Mason, P. E.; Jungwirth, P. Ion Pairing in Aqueous Lithium Salt Solutions with Monovalent and Divalent Counter-Anions. *J. Phys. Chem. A* **2013**, *117* (46), 11766–11773. https://doi.org/10.1021/jp402532e.

(11) Pluhařová, E.; Fischer, H. E.; Mason, P. E.; Jungwirth, P. Hydration of the Chloride Ion in Concentrated Aqueous Solutions Using Neutron Scattering and Molecular Dynamics. *Molecular Physics* **2014**, *112* (9–10), 1230–1240. https://doi.org/10.1080/00268976.2013.875231.

(12)Roget, S. A.; Carter-Fenk, K. A.; Fayer, M. D. Water Dynamics and Structure of Highly Concentrated LiCl Solutions Investigated Using Ultrafast Infrared Spectroscopy. *J. Am. Chem. Soc.* **2022**, *144* (9), 4233–4243. https://doi.org/10.1021/jacs.2c00616.
(13)Pethes, I. A Comparison of Classical Interatomic Potentials Applied to Highly Concentrated Aqueous Lithium Chloride Solutions. *Journal of Molecular Liquids* **2017**, *242*, 845–858. https://doi.org/10.1016/j.molliq.2017.07.076.